Pressure-induced structural changes in the network-forming isostatic glass $GeSe_4$: An investigation by neutron diffraction and first-principles molecular dynamics

Assil Bouzid,[1] Keiron J. Pizzey,[2] Anita Zeidler,[2] Guido Ori,[1] Mauro Boero,[1] Carlo Massobrio,[1] Stefan Klotz,[3] Henry E. Fischer,[4] Craig L. Bull,[5] and Philip S. Salmon[2,*]

[1]*Institut de Physique et Chimie des Matériaux de Strasbourg, Département de Chimie des Matériaux Inorganiques 23, rue du Loess, BP 43, F-67034 Strasbourg Cedex 2, France*

[2]*Department of Physics, University of Bath, Bath BA2 7AY, United Kingdom*

[3]*IMPMC, CNRS UMR 7590, Université Pierre et Marie Curie, F-75252 Paris, France*

[4]*Institut Laue-Langevin, 6 rue Jules Horowitz, BP 156, F-38042 Grenoble Cédex 9, France*

[5]*ISIS Facility, Rutherford Appleton Laboratory, Chilton, Didcot, Oxon OX11 0QX, United Kingdom*

(Received 19 July 2015; revised manuscript received 21 December 2015; published 15 January 2016)

The changes to the topological and chemical ordering in the network-forming isostatic glass $GeSe_4$ are investigated at pressures up to ∼14.4 GPa by using a combination of neutron diffraction and first-principles molecular dynamics. The results show a network built from corner- and edge-sharing $Ge(Se_{1/2})_4$ tetrahedra, where linkages by Se_2 dimers or longer Se_n chains are prevalent. These linkages confer the network with a local flexibility that helps to retain the network connectivity at pressures up to ∼8 GPa, corresponding to a density increase of ∼37%. The network reorganization at constant topology maintains a mean coordination number $\bar{n} \simeq 2.4$, the value expected from mean-field constraint-counting theory for a rigid stress-free network. Isostatic networks may therefore remain optimally constrained to avoid stress and retain their favorable glass-forming ability over a large density range. As the pressure is increased to around 13 GPa, corresponding to a density increase of ∼49%, $Ge(Se_{1/2})_4$ tetrahedra remain as the predominant structural motifs, but there is an appearance of 5-fold coordinated Ge atoms and homopolar Ge-Ge bonds that accompany an increase in the fraction of 3-fold coordinated Se atoms. The band gap energy decreases with increasing pressure, and midgap states appear at pressures beyond ∼6.7 GPa. The latter originate from undercoordinated Se atoms that terminate broken Se_n chains.

DOI: 10.1103/PhysRevB.93.014202

I. INTRODUCTION

Ge_xSe_{1-x} $(0 \leqslant x \leqslant 1)$ is an archetypal network glass-forming system that has been a focus of considerable attention, partly because of its role in providing essential building blocks for chalcogenide glasses with optoelectronic, infrared-optical, and acousto-optical applications [1–9], and partly because of its role as a prototype in helping to understand the atomic-scale structural organization of disordered networks [10–26]. Here, the wide glass-forming region $(0 \leqslant x \leqslant 0.43)$ [27] indicates that homopolar (i.e., Ge-Ge or Se-Se) bonds are important network features, and topological constraint-counting ideas provide a guide for predicting the composition dependence of structure-related properties that include the glass-forming tendency [28,29]. According to mean-field constraint-counting theory, a systematic increase of x will lead to the change from an elastically "floppy" or underconstrained network to a "stressed-rigid" or overconstrained network, via a single composition at $x = 0.2$ for which the network is rigid or "isostatic." At this composition, the number of constraints per atom is equal to the number of degrees of freedom per atom, glass-forming tendency is optimal, and the mean nearest-neighbor coordination number $\bar{n} = 2.4$. Spectroscopic and calorimetric studies do point, however, to a transition region known as the intermediate phase, i.e., to a finite interval of compositions near $x = 0.2$ that separates the floppy from the stressed-rigid regimes [30–32]. Within the intermediate phase, a network is deemed to self-organize on formation to give a rigid system that is optimally constrained to avoid stress.

Pressure provides a means for tuning the properties of a network at constant composition and, accordingly, there have been several investigations of the Ge_xSe_{1-x} system. For example, the pressure-dependent properties of the stressed-rigid glass $GeSe_2$ have been probed by x-ray and neutron diffraction [33–36], x-ray absorption spectroscopy [36], Raman spectroscopy [37,38], sound velocity [39], electrical conductivity [40,41], and first-principles molecular dynamics (FPMD) [34,42] methods. It is unclear, however, as to whether there is an abrupt semiconductor-glass to metal-crystal transition [40,41], or a gradual evolution in the structure to give a more metallic glass [33–36,42], the details of which may be sensitive to the thermal history [34]. At pressures below ∼8.5 GPa, neutron diffraction and FPMD results reveal a self-consistent picture in which there is no change to $\bar{n}$ but a trade-off between the fractions of corner- and edge-sharing tetrahedra with increasing density. At pressures beyond this threshold, the FPMD results show an increase in $\bar{n}$ that is more rapid than found from diffraction, where homopolar bonds play a mediating role in the appearance of higher coordinated Ge and Se atoms [34,35]. The pressure-dependent properties of the isostatic glass $GeSe_4$ have also been probed by x-ray diffraction [43,44], Raman spectroscopy [44], and electrical conductivity [40,41,44] methods. A discontinuous increase in the electrical conductivity is reported at a pressure that accompanies the transformation from a low-density semiconducting glass to either a high-density metallic glass in the range 10–12 GPa (Ref. [44]) or a metallic crystal at

*Corresponding author: p.s.salmon@bath.ac.uk

∼10.5 GPa [40,41]. There is disagreement, however, between the x-ray diffraction results regarding the pressure-dependent structure, e.g., in respect to the rate of change of $\bar{n}$ with increasing density [43,44].

We have therefore been motivated to investigate the structure of $GeSe_4$ glass at room temperature and pressures up to ∼14.4 GPa by using the method of *in situ* high-pressure neutron diffraction [35]. The experimental work is complemented by a set of Car-Parrinello [45] FPMD simulations that give an accurate account of the atomic-scale structure in the Ge_xSe_{1-x} family of network-forming materials, as indicated by detailed comparisons with experiment for compositions that include GeSe [46,47], Ge_2Se_3 [17,48–50], $GeSe_2$ [26,34,51–58], $GeSe_4$ [26,56,59–62], and $GeSe_9$ [26,63]. The combined techniques yield a self-consistent picture for $GeSe_4$ glass over the entire pressure range in which there is little change to the topological and chemical ordering at pressures up to ∼8 GPa. Isostatic networks may therefore maintain their optimal glass-forming characteristics over a wide pressure range.

The paper is organized as follows. The essential theory for neutron and x-ray diffraction experiments is given in Sec. II. The experimental and FPMD methods are then described in Secs. III and IV, respectively. The results are presented in Sec. V and the densification mechanisms are discussed in Sec. VI. Conclusions are drawn in Sec. VII.

II. THEORY

In a neutron or x-ray diffraction experiment on $GeSe_4$ glass the total structure factor

$$S(k) = 1 + \frac{1}{|\langle f(k)\rangle|^2}\sum_{\alpha=1}^{n}\sum_{\beta=1}^{n} c_\alpha c_\beta f_\alpha(k) f_\beta^*(k)[S_{\alpha\beta}(k) - 1] \tag{1}$$

is measured, where α and β denote the chemical species, n is the number of different chemical species, c_α represents the atomic fraction of chemical species α, $f_\alpha(k)$ and $f_\alpha^*(k)$ are the form factor (or scattering length) for chemical species α and its complex conjugate, respectively, $\langle f(k)\rangle = c_{\rm Ge} f_{\rm Ge}(k) + c_{\rm Se} f_{\rm Se}(k)$ is the mean form factor, and k is the magnitude of the scattering vector [64]. The k dependence of the form factors is important in x-ray diffraction experiments, but can be neglected in neutron diffraction experiments. In Eq. (1), information on the glass structure is contained in the Faber-Ziman [65] partial structure factors $S_{\alpha\beta}(k)$, which are related to the partial pair-distribution functions $g_{\alpha\beta}(r)$ via the Fourier transform relation

$$g_{\alpha\beta}(r) = 1 + \frac{1}{2\pi^2 \rho\, r}\int_0^\infty dk\, k\,[S_{\alpha\beta}(k) - 1]\sin(kr), \tag{2}$$

where ρ is the atomic number density and r is a distance in real space. The mean coordination number of atoms of type β, contained in a volume defined by two concentric spheres of radii r_i and r_j centered on an atom of type α, is given by

$$\bar{n}_\alpha^\beta = 4\pi\, \rho\, c_\beta \int_{r_i}^{r_j} dr\, r^2 g_{\alpha\beta}(r). \tag{3}$$

The real-space information corresponding to Eq. (1) is provided by the total pair-distribution function

$$G(r) = 1 + \frac{1}{2\pi^2 \rho\, r}\int_0^\infty dk\, k\,[S(k) - 1]M(k)\sin(kr), \tag{4}$$

where $M(k)$ is a modification function defined by $M(k) = 1$ for $k \leqslant k_{\rm max}$, $M(k) = 0$ for $k > k_{\rm max}$. The latter is introduced because a diffractometer can measure only over a finite scattering vector range up to a maximum value $k_{\rm max}$. To facilitate a comparison between the FPMD and experimental results, the reciprocal-space functions constructed from the simulations were Fourier transformed according to Eq. (4) with $k_{\rm max}$ set at the experimental value. The severity of Fourier transform artifacts can be reduced by using a Lorch [66] modification function in Eq. (4), albeit at the expense of broadened features such as the first peak in $G(r)$, where $M(k) = \sin(ak)/(ak)$ for $k \leqslant k_{\rm max}$, $a \equiv \pi/k_{\rm max}$, and $M(k) = 0$ for $k > k_{\rm max}$ [67].

The total structure factor of Eq. (1) can also be written in terms of the Bhatia-Thornton [68] partial structure factors that separate the structural information into its contributions from the topological and chemical ordering, and their cross-correlation. In x-ray diffraction experiments on $GeSe_4$ glass the similarity between the atomic numbers of Ge and Se means that $f_{\rm Ge}(k) \simeq f_{\rm Se}(k)$, and in neutron diffraction experiments on $GeSe_4$ glass made from elements having their naturally occurring isotopic abundance $f_{\rm Ge} \simeq f_{\rm Se}$. Thus, $S(k) \simeq S_{\rm NN}(k)$ and $G(r) \simeq g_{\rm NN}(r)$ to an excellent level of approximation [17], where $S_{\rm NN}(k)$ denotes the Bhatia-Thornton number-number partial structure factor and $g_{\rm NN}(r)$ its corresponding Fourier transform. These functions describe the pair correlations between the sites of the scattering centers in a diffraction experiment but, because of the form-factor similarity, the x-rays or neutrons cannot distinguish between the chemical species that occupy those sites; i.e., the measured functions give information on the topological ordering alone. From the definition of the number-number partial pair-distribution function

$$g_{\rm NN}(r) \equiv c_{\rm Ge}^2 g_{\rm GeGe}(r) + c_{\rm Se}^2 g_{\rm SeSe}(r) + 2c_{\rm Ge}c_{\rm Se}g_{\rm GeSe}(r), \tag{5}$$

it follows that the mean coordination number $\bar{n}$ is given by

$$\bar{n} = 4\pi\rho\int_{r_i}^{r_j} dr\, r^2 g_{\rm NN}(r) = c_{\rm Ge}\bar{n}_{\rm Ge} + c_{\rm Se}\bar{n}_{\rm Se}, \tag{6}$$

where $\bar{n}_{\rm Ge} \equiv \bar{n}_{\rm Ge}^{\rm Ge} + \bar{n}_{\rm Ge}^{\rm Se}$ and $\bar{n}_{\rm Se} \equiv \bar{n}_{\rm Se}^{\rm Se} + \bar{n}_{\rm Se}^{\rm Ge}$ are the mean Ge and Se coordination numbers, respectively. According to the "8-N" rule, $\bar{n} = 2.4$ for the $GeSe_4$ composition. A full description of the Bhatia-Thornton formalism as applied to binary network glass-forming systems is given elsewhere [69,70].

In the following, the notation $S_{\rm N}(k)$ and $S_{\rm X}(k)$ will be used in order to distinguish between the total structure factors measured by neutron and x-ray diffraction, and the corresponding total pair-distribution functions will be denoted by $G_{\rm N}(r)$ and $G_{\rm X}(r)$, respectively. For the case of a neutron diffraction experiment on $GeSe_4$ glass using Ge and Se of natural isotopic abundance, the (k-independent) coherent neutron scattering lengths are $f_{\rm Ge} = 8.185(20)$ fm and $f_{\rm Se} = 7.970(9)$ fm, respectively [71]. Then, the relative weighting factors for the Ge-Ge, Ge-Se, and Se-Se $S_{\alpha\beta}(k)$ functions are 0.0417 : 0.3251 : 0.6332 for neutron diffraction versus

0.0363 : 0.3084 : 0.6553 for x-ray diffraction at $k = 0$. Thus, the measured diffraction patterns are most sensitive to the Se-Se correlations and least sensitive to the Ge-Ge correlations.

III. EXPERIMENTAL

Glassy samples were prepared by loading elemental Ge (99.9998%, Sigma-Aldrich) and Se (99.999%, Sigma-Aldrich) of natural isotopic abundance into a silica ampoule (4 mm or 6 mm inner diameter depending on the desired sample diameter, and 1 mm wall thickness) that had been etched using a 48 wt. % solution of hydrofluoric acid, rinsed using acetone, and baked dry under vacuum at 1073 K for 3 h. The ampoule was loaded in a high-purity argon-filled glove box, isolated using a Young's tap, and then transferred to a vacuum line where it was sealed under a pressure of 10^{-5} Torr. The sealed ampoule was placed in a rocking furnace, which was heated at a rate of 2 K min^{-1} from ambient to a temperature $T = 1248$ K, dwelling for 4 h each at $T = 494$ K and $T = 958$ K, near the melting and boiling points of Se, respectively. For the sample made in the 6 mm ampoule, an additional dwell was made at 1211 K for 4 h, near the melting point of Ge. The highest temperature was maintained for 48–51 h before the rocking motion was stopped, the furnace was placed vertically, and was then cooled at a rate of 2 K min^{-1} to $T = 1027$ K where the sample was left to equilibrate for 4–5 h. The ampoule was then dropped into an ice/water mixture, annealed for 2 h at $T = 403$ K [below the glass transition temperature of $T_g = 455(2)$ K as measured using modulated differential scanning calorimetry with a scan rate of 3 K min^{-1} and modulation of 1 K per 100 s], and sectioned using a diamond-wire saw to prepare $GeSe_4$ glass cylinders. The infrared transmission spectra measured for the glass showed no indication of Ge-O or Se-O impurity bands, e.g., in the region around 735–781 cm^{-1} [72]. The glass cylinders were gently ground (by using a rotary tool in a dry Ar-filled glove bag) into the correct shape for either a single- or double-toroid anvil geometry.

The high-pressure neutron diffraction experiments were made using a Paris-Edinburgh press [73] at ambient temperature ($T \sim 300$ K) using either the diffractometer D4c at the steady-state reactor source of the Institut Laue-Langevin with an incident neutron wavelength of 0.4985(1) Å [74] or the time-of-flight diffractometer PEARL at the ISIS pulsed neutron source. The samples were held in gaskets made from the null-scattering alloy $Ti_{0.676}Zr_{0.324}$ for which the pressure-volume equation of state used in the data analysis was taken from Ref. [75]. The D4c diffraction experiments were performed at ambient pressure, 3.0(5), 4.7(5), 6.3(5), 7.0(5), and 8.1(5) GPa using a single-toroid anvil geometry, and the PEARL diffraction experiments were performed at 8.7(5), 10.9(5), 12.8(5), and 14.4(5) GPa using a double-toroid anvil geometry. The pressure versus load calibration curves were taken from Ref. [77], and the measurement and data analysis procedures are described in detail elsewhere [35,76–78]. In the case of the PEARL experiments, the data analysis procedure employed a Lorentzian function to extrapolate a measured $S_N(k)$ function to $k = 0$ for use in Eq. (4) [77].

An additional diffraction experiment was performed on $GeSe_4$ glass at ambient pressure using the D4c instrument with an incident neutron wavelength of 0.5003(1) Å. A powdered glass sample was held in a vanadium container of 4.8 mm inner diameter and 0.1 mm wall thickness, thus reducing the container scattering in comparison to a Paris-Edinburgh press experiment. Diffraction patterns were measured for the sample in its container, the empty container, the empty instrument, and a cylindrical vanadium rod of diameter 6.072(6) mm for normalization purposes. A diffraction pattern was also measured for a bar of neutron absorbing $^{10}B_4C$ of dimensions comparable to the sample to account for the effect of sample attenuation on the background signal at small scattering angles. The data analysis followed the procedure described in Ref. [79].

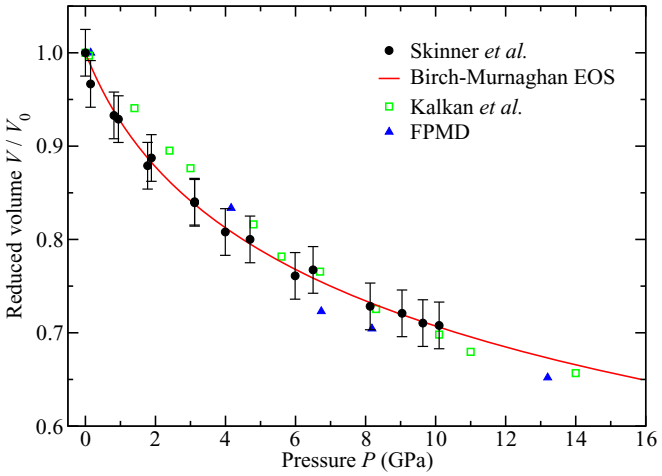

FIG. 1. The pressure-volume equation of state for amorphous $GeSe_4$ as measured under compression in the experiments of Skinner *et al.* [43] [solid (black) circles with vertical error bars] and Kalkan *et al.* [44] [open (green) squares]. The solid (red) curve gives a fit to the data of Ref. [43] using a third-order Birch-Murnaghan equation of state (Sec. III), and the solid (blue) triangles give the FPMD results from the present work.

The number density of $GeSe_4$ glass at ambient pressure was measured to be $\rho_0 = 0.0335(1)$ Å^{-3} by using a helium pycnometer. At higher pressures, ρ was taken from a fit to the measured pressure dependence of the reduced volume V/V_0 for $GeSe_4$ glass under cold compression (Fig. 1) [43], by using a third-order Birch-Murnaghan equation of state [80]:

$$P = (3B_0/2)[(V/V_0)^{-7/3} - (V/V_0)^{-5/3}] \times \{1 + (3/4)(B_0' - 4)[(V/V_0)^{-2/3} - 1]\}, \quad (7)$$

where V is the volume at pressure P and V_0 is the volume at zero pressure. This fit gave an isothermal bulk modulus $B_0 = 10.42(69)$ GPa and pressure derivative $B_0' = 5.96(52)$, where the former compares to an ambient pressure adiabatic bulk modulus of 11.6 GPa (Ref. [81]) or 11.47 GPa (Ref. [82]) as obtained from sound velocity measurements on $GeSe_4$ glass.

In Fig. 1, it is important to note that the V/V_0 data taken from Ref. [44] correspond to a single value for V_0 that originates from an ambient pressure number density $\rho_0 = 0.0333$ Å^{-3}. The equation-of-state results do, however, point to the transition from a low-density amorphous to a high-density amorphous phase at a pressure ~10.1 GPa, which leads to a discontinuity in the plot of P versus V/V_0 shown in Ref. [44]; i.e., the high-density amorphous phase was assumed

to correspond to a different value of V_0. For the low-density amorphous phase, a fit to the data using a third-order Birch-Murnaghan equation of state gives $B_0 = 18.0(3.2)$ GPa and $B_0' \sim 2.7$ [44].

IV. FIRST-PRINCIPLES MOLECULAR DYNAMICS SIMULATIONS

The simulations were performed using the Car-Parrinello [45] method as implemented in the CPMD computer code [83] with $N = 120$ atoms in a periodically repeated cubic cell. A generalized gradient approximation (GGA) with the Becke-Lee-Yang-Parr (BLYP) functional [84,85] was used to describe the electron exchange and correlation part of the total energy. Valence electrons were treated explicitly and were represented by a plane-wave basis set expanded at the Γ point of the simulation cell with an energy cutoff of 20 Ry. The valence-core interactions were described by norm-conserving pseudopotentials of the Troullier-Martins type [86]. The largest cutoff used in the pseudopotential construction was equal to 1.06 Å. A fictitious electron mass of 1000 a.u. (i.e., in units of $m_e a_0^2$ where m_e is the electron mass and a_0 is the Bohr radius) and a time step of $\Delta t = 0.24$ fs were used to integrate the equations of motion, ensuring good control of the conserved quantities. The temperature for both the ionic and electronic degrees of freedom was controlled by a Nosé-Hoover thermostat [87–90].

Previous work on amorphous $GeSe_2$ under ambient conditions has emphasized the important role of residual pressure on the glass structure [58]. Thus, an initial equilibrated configuration for $GeSe_4$ glass at $T = 300$ K was taken from the model studied in Ref. [60], and by reducing the density (within the NVT ensemble) from 0.035 $Å^{-3}$ (Ref. [60]) to 0.03122 $Å^{-3}$, the internal pressure was lowered to $\lesssim$0.15 GPa. A simulation was also performed in the isobaric (NPT) ensemble using the Parrinello-Rahman method, allowing only for an isotropic variation of the cell dimensions [91–93], with the fictitious mass parameter fixed at 10^8 a.u. to ensure stability of the cell dynamics. This run gave an ambient pressure density that oscillated around an equilibrium value of 0.03111 $Å^{-3}$. The resultant configuration was taken as the starting point for each high-pressure simulation.

Simulations were also performed using the NPT ensemble at high pressures of 4.15, 8.18, and 13.2 GPa. For each of these state points, as well as for the simulation made at ambient pressure, the system was taken on a thermal cycle, starting at $T = 100$–400 K for 18–37 ps, increasing to $T = 600$ K for 10–50 ps and then to $T = 900$–1100 K for 28–133 ps, decreasing to $T = 600$ K for 26–48 ps, and finishing at 300 K for 50–81 ps, where the temperature bands refer to 2–3 temperature plateaus and the associated times are cumulative. Substantial diffusion at the highest temperature on the scale of several interatomic distances ensured that no memory was kept of an initial configuration such that the simulated glasses produced under pressure were statistically uncorrelated. Statistical averages were taken from the final 50 ps portion of the relaxed $T = 300$ K trajectory at the end of a thermal cycle. A simulation using the NVT ensemble was also performed with a similar thermal cycle at a pressure of 6.73 GPa. The modeled equation of state is in accord with experiment [43,44] within the measurement error (Fig. 1).

To establish the pressure-dependent relation between the atomic and electronic structures of the glassy network, we calculated the electronic density of states (EDOS), the maximally localized Wannier functions [94,95], and the weighted centers of the Wannier function charge distributions, i.e., the Wannier function centers (WFCs).

Following a standard procedure, the Wannier functions and corresponding centers were obtained by an *on the fly* unitary transformation of the Kohn-Sham orbitals $\psi_i(\mathbf{r})$, where $\mathbf{r}$ denotes a real-space coordinate for the ith orbital. Specifically, of all possible unitary transformations, we selected the one that minimizes the spread (spatial extent) Ω of the resulting Wannier orbitals $w_n(\mathbf{r})$, where

$$\Omega = \sum_n (\langle w_n|\mathbf{r}^2|w_n\rangle - \langle w_n|\mathbf{r}|w_n\rangle^2) \tag{8}$$

and n is an index that labels each of the Wannier orbitals. This approach leads to an iterative scheme for computing the orbital transformation

$$w_n(\mathbf{r}) = \sum_i \left[\prod_p \exp\left(-A_{i,n}^p\right)\cdot \psi_i(\mathbf{r})\right], \tag{9}$$

where $A_{i,n}^p$ is a matrix generalization of the Berry phase connector, and p is the order of the iteration as specified in Ref. [95]. In this way, the Wannier states provide an unbiased method for partitioning the charge density, and information on the bonding is contracted into four numbers, i.e., the Cartesian coordinates x_n, y_n, and z_n of the nth WFC and its spread Ω. The center of an orbital along the x direction is defined by

$$x_n = -\frac{L_x}{2\pi}\mathrm{Im}\ln\langle w_n|\exp(-i2\pi\cdot x/L_x)|w_n\rangle, \tag{10}$$

where L_x is the length of the simulation cell along the x direction. Similar expressions hold for the other two Cartesian coordinates of a WFC.

An analysis of the local electronic structure in terms of maximally localized Wannier functions and WFCs has helped to elucidate the nature of the chemical bonding in several disordered chalcogenide materials [25,50,62,96].

V. RESULTS

A. Diffraction results

Figure 2 compares the $S_N(k)$ functions measured in the present work with the $S_X(k)$ functions measured by Skinner *et al.* [43] and Kalkan *et al.* [44], which are expected to be similar because $S_N(k) \simeq S_X(k) \simeq S_{NN}(k)$ (Sec. II). Good agreement is found between the $S_N(k)$ functions and the $S_X(k)$ functions taken from Ref. [43], where a sharpening of peaks in the x-ray diffraction data at ambient pressure can be attributed to the use of a diffractometer with a sharper resolution function [97]. The $S_X(k)$ functions from Ref. [44], which correspond to a reduced k-space range of $0.8 \leqslant k\ (Å^{-1}) \leqslant 9$, are in fair accord with the other data sets. As the pressure is increased from ambient, the first sharp diffraction peak (FSDP) at $\simeq$1.12 $Å^{-1}$ shifts to larger k and broadens, and is difficult to discern at

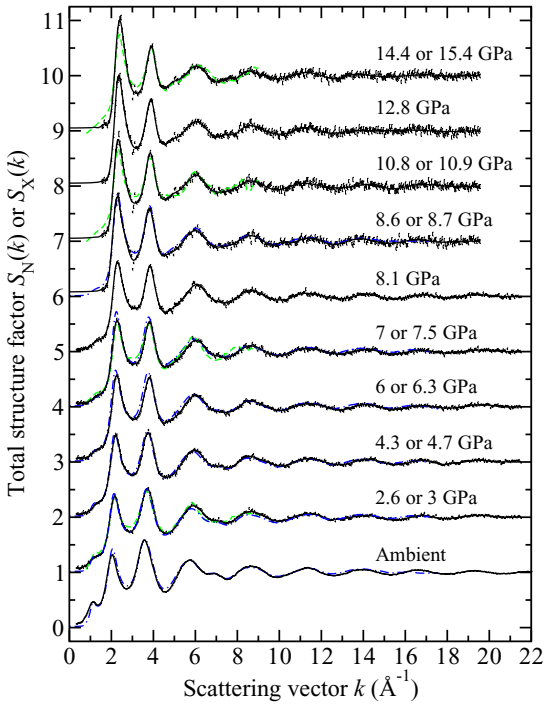

FIG. 2. The pressure dependence of the neutron total structure factor $S_N(k)$ and x-ray total structure factor $S_X(k)$ for $GeSe_4$ glass where $S_N(k) \simeq S_X(k) \simeq S_{NN}(k)$. The points with vertical error bars give the $S_N(k)$ functions measured in the present work at ambient pressure (using a vanadium container), 3, 4.7, 6.3, 7, 8.1, 8.7, 10.9, 12.8, and 14.4 GPa. The solid (black) curves show spline fits to these functions, except in the region $k \leqslant 1.55$ Å^{-1} for the 8.7–14.4 GPa data sets where they correspond to fitted Lorentzian functions (Sec. III). The chained (blue) curves give the $S_X(k)$ functions measured by Skinner *et al.* [43] at ambient pressure, 3, 4.3, 6, 7, and 8.6 GPa, and the broken (green) curves give the $S_X(k)$ functions measured by Kalkan *et al.* [44] at 2.6, 7.5, 10.8, and 15.4 GPa. The high-pressure curves have been offset vertically for clarity of presentation.

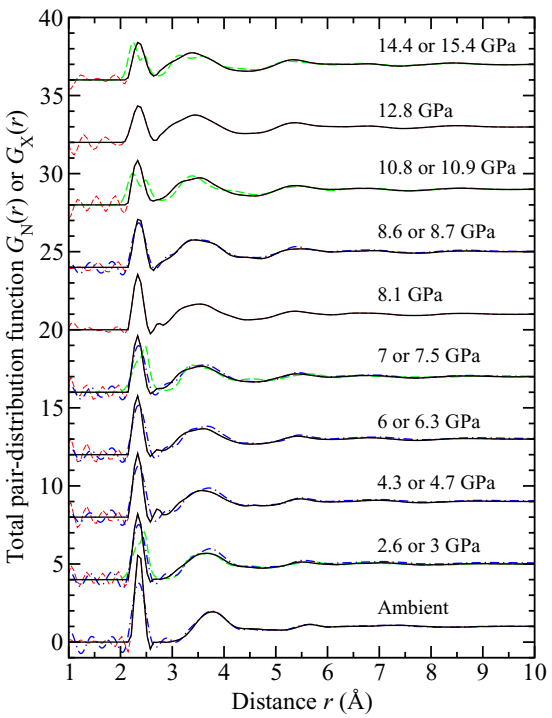

FIG. 3. The pressure dependence of the neutron total pair-distribution function $G_N(r)$ and x-ray total pair-distribution function $G_X(r)$ for $GeSe_4$ glass where $G_N(r) \simeq G_X(r) \simeq g_{NN}(r)$. The solid (black) curves give the Fourier transforms of spline fits to the $S_N(k)$ functions shown by the solid (black) curves in Fig. 2 at ambient pressure, 3, 4.7, 6.3, 7, 8.1, 8.7, 10.9, 12.8, and 14.4 GPa. The chained (red) curves show the Fourier transform artifacts at r values smaller than the distance of closest approach between two atoms, and oscillate about the calculated $G_N(r \to 0) = 0$ limiting values as shown by the solid (black) curves in the small-r region. The chained (blue) curves give the Fourier transforms of the $S_X(k)$ functions shown by the chained (blue) curves in Fig. 2 at ambient pressure, 3, 4.3, 6, 7, and 8.6 GPa [43]. The broken (green) curves give the $g_{NN}(r)$ functions at 2.6, 7.5, 10.8, and 15.4 GPa that were constructed by using Eq. (5) to combine the $g_{\alpha\beta}(r)$ functions that were obtained from the EPSR method [44]. The high-pressure curves have been offset vertically for clarity of presentation.

pressures above 8 GPa. At the same time, the principal peak at $\simeq$2.04 Å^{-1} sharpens and shifts to $\simeq$2.40 Å^{-1} at 14.4 GPa.

A comparison of the $G_N(r)$ functions from the present work and the $G_X(r)$ functions from Ref. [43] is given in Fig. 3 where $G_N(r) \simeq G_X(r) \simeq g_{NN}(r)$. The neutron diffraction results were obtained from the spline-fitted $S_N(k)$ functions shown in Fig. 2 by using Eq. (4) with either (i) a step modification function or (ii) a Lorch modification function. The data obtained from the second procedure were joined smoothly to the data obtained from the first procedure at a point just beyond the first peak in $G_N(r)$. There is general accord between the $G_N(r)$ and $G_X(r)$ functions, although there is a broadening of the first peak in $G_X(r)$ at pressures below 8 GPa that can be attributed to the use in Eq. (4) of a reduced value of $k_{max} \simeq 17.2$ Å^{-1} relative to $k_{max} = 23.45$ Å^{-1} (ambient pressure) or $k_{max} = 21.5$ Å^{-1} (high pressures) in the D4c neutron diffraction study. In the work by Kalkan *et al.* [44], the full set of $g_{\alpha\beta}(r)$ functions was obtained by using the empirical potential structure refinement (EPSR) method [98] in which their measured $S_X(k)$ functions (Fig. 2) were used as a reference. The $g_{\alpha\beta}(r)$ functions thus obtained were combined by using Eq. (5) to give the $g_{NN}(r)$ functions shown in Fig. 3. The latter show a split first peak in real space, in contrast to the $G_X(r)$ functions obtained by direct Fourier transformation of the measured $S_X(k)$ functions with $k_{max} = 9$ Å^{-1} [44]; i.e., the split peak appears to originate from the constraints applied in the modeling procedure.

To identify the length scales on which the main structural changes occur, it is helpful to amplify the large-r features by constructing the difference function $\Delta D_N(r) = D_N(r) - D_N^0(r)$ where the density pair-correlation function at a high-pressure point is given by $D_N(r) \equiv 4\pi\rho\, r\, [G_N(r) - 1]$ and $D_N^0(r)$ is the density pair-correlation function at ambient pressure. Figure 4 shows that as the pressure is increased from ambient there is a decrease in height and broadening of the first peak in $D_N(r)$ that is initially at 2.36(1) Å, a shift to low r and broadening of the second peak that is initially at 3.77(1) Å, and a shift to low r and increase in prominence of the third peak that is initially at 5.59(1) Å. Although the first peak broadens it does not, however, lead to a marked change

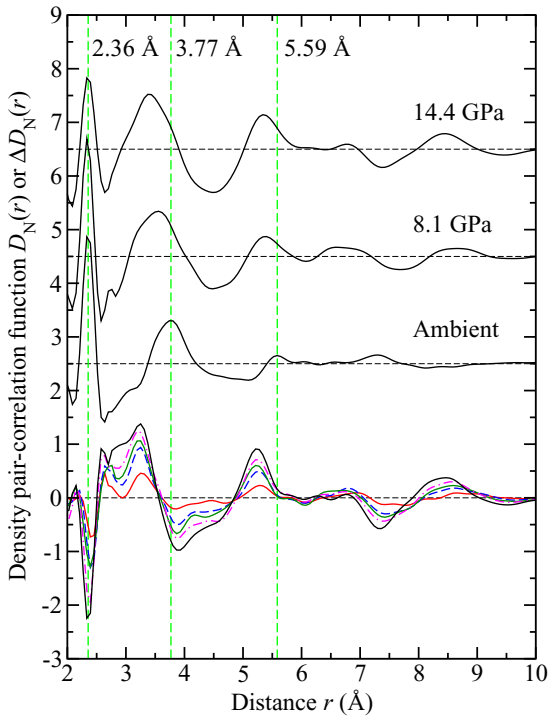

FIG. 4. The density pair-correlation function $D_N(r)$ for $GeSe_4$ glass as measured using neutron diffraction at ambient pressure, 8.1 and 14.4 GPa. The difference function $\Delta D_N(r)$ is also plotted for high pressures corresponding to 3 GPa [solid (red) curve], 6.3 GPa [broken (blue) curve], 8.1 GPa [solid (green) curve], 10.9 GPa [chained (magenta) curve], and 14.4 GPa [solid (black) curve]. The vertical broken lines give the first three peak positions in the ambient-pressure density pair-correlation function, and the $D_N(r)$ curves have been offset vertically for clarity of presentation.

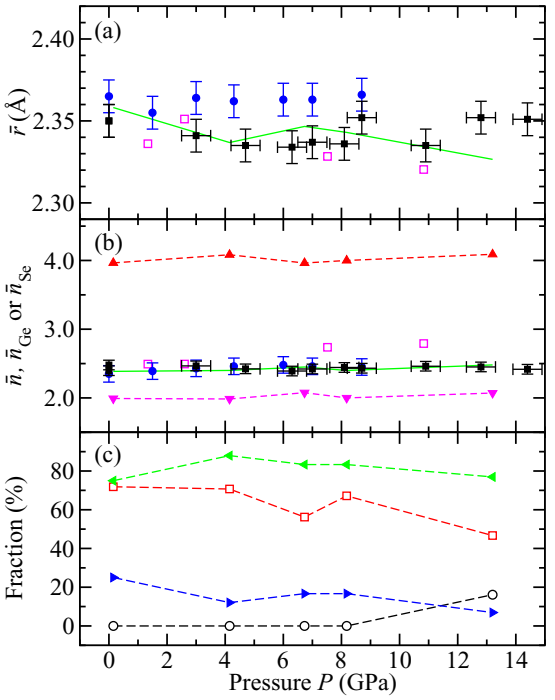

FIG. 5. The pressure dependence of (a) the mean nearest-neighbor distance $\bar{r}$ as measured in (i) the x-ray diffraction work of Skinner *et al.* [43] [(blue) solid circles with vertical error bars] and Kalkan *et al.* [44] [(magenta) open squares], (ii) the present neutron diffraction work [(black) solid squares with error bars], and (iii) as calculated by FPMD [solid (green) curve]; (b) the mean coordination number $\bar{n}$ as measured in (i) the x-ray diffraction work of Skinner *et al.* [43] [(blue) solid circles with vertical error bars] and Kalkan *et al.* [44] [(magenta) open squares], (ii) the present neutron diffraction work [(black) solid squares with error bars], and (iii) as calculated by FPMD [solid (green) curve], where the latter is broken down into its contributions from $\bar{n}_{Ge}$ [(red) upward-pointing triangles] and $\bar{n}_{Se}$ [(magenta) downward-pointing triangles]; and (c) the FPMD results for the fractions of Ge [(black) open circles] and Se [(red) open squares)] atoms involved in homopolar bonds, and the fractions of Ge atoms involved in corner-sharing [(green) leftward-pointing triangles] and edge-sharing [(blue) rightward-pointing triangles] tetrahedra.

in $\bar{n}$ over the measured pressure range, in agreement with the x-ray diffraction results from Ref. [43] but in contrast to the x-ray diffraction results from Ref. [44] which show an increase in $\bar{n}$ from $\simeq$2.5 at 1.34 GPa to $\simeq$2.8 at 10.83 GPa [Fig. 5(b)].

B. FPMD results

The pressure dependence of the simulated and measured neutron total structure factors is given in Fig. 6, and the corresponding real-space functions are shown in Fig. 7. The simulations account for all of the main features in the measured data sets over the entire pressure range. The modeled $\bar{r}$ values capture the initial pressure-induced bond contraction observed by neutron diffraction and by x-ray diffraction in the work from Ref. [44] [Fig. 5(a)], and the modeled $\bar{n}$ values show very little change with pressure, as observed by neutron diffraction and by x-ray diffraction in the work from Ref. [43] [Fig. 5(b)].

Figure 8 shows the pressure dependence of the simulated partial structure factors $S_{\alpha\beta}(k)$ that were obtained by Fourier-transforming the partial pair-distribution functions $g_{\alpha\beta}(r)$ shown in Fig. 9. At ambient pressure, the FSDP in the total structure factor at $k \simeq 1.12\,\text{Å}^{-1}$ originates from the Ge-Ge and Ge-Se correlations, as found for the case of glassy $GeSe_2$ [53,54], and the principal peak at $k \simeq 2.04\,\text{Å}^{-1}$ originates from a combination of peaks in $S_{GeGe}(k)$ and $S_{SeSe}(k)$ that are offset by a trough in $S_{GeSe}(k)$. As the pressure is increased, the FSDP in $S_{GeGe}(k)$ decreases in height and shifts to higher-k values, whereas the changes to the FSDP in $S_{GeSe}(k)$ are less pronounced. The increase with pressure in height of the principal peak in the total structure factor originates mainly from the principal peak in $S_{SeSe}(k)$.

The pressure evolution of the partial pair-distribution functions $g_{\alpha\beta}(r)$ is shown in Fig. 9. At ambient pressure, the first peak at $\simeq$2.35 Å in $G_N(r)$ or $G_X(r)$ originates from Ge-Se and Se-Se correlations with $\bar{n}_{Ge} = 4$ and $\bar{n}_{Se} = 2$ [Fig. 5(b)], where the partial coordination numbers $\bar{n}_\alpha^\beta$ that contribute to $\bar{n}_{Ge}$ and $\bar{n}_{Se}$ were computed by using Eq. (3) to integrate over the first peak in the relevant $g_{\alpha\beta}(r)$ function. The absence of homopolar Ge-Ge bonds [Fig. 5(c)] implies that $\bar{n}_{Ge} = \bar{n}_{Ge}^{Se} = 4$, a value that is consistent with the formation of $Ge(Se_{1/2})_4$ tetrahedral motifs. The coordination numbers show little variation with pressure, increasing to $\bar{n}_{Ge} \simeq 4.1$ and $\bar{n}_{Se} \simeq 2.1$ at 13.2 GPa, corresponding to an increase in the mean coordination number $\bar{n}$ from $\simeq$2.39 at 0.15 GPa to $\simeq$2.48 at 13.2 GPa [Fig. 5(b)]. At the highest pressure,

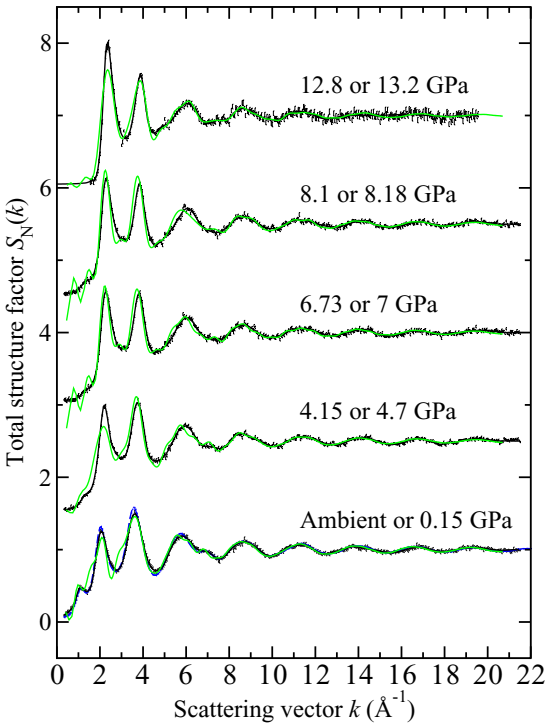

FIG. 6. The pressure dependence of the neutron total structure factor $S_N(k)$ as measured for $GeSe_4$ glass using a Paris-Edinburgh press at ambient pressure, 4.7, 7, 8.1, and 12.8 GPa (points with vertical error bars), and as calculated by Fourier-transforming the FPMD real-space total pair-distribution functions at 0.15, 4.15, 6.73, 8.18, and 13.2 GPa [solid light (green) curves]. The solid (black) curves show spline fits to the measured data sets, except in the region $k \leqslant 1.55$ Å^{-1} for the 12.8 GPa pressure point where it corresponds to a fitted Lorentzian function (Sec. III). The chained (blue) curve at ambient pressure corresponds to the data obtained from a separate neutron diffraction experiment in which the sample was held in a vanadium container (Sec. III). The high-pressure curves have been offset vertically for clarity of presentation.

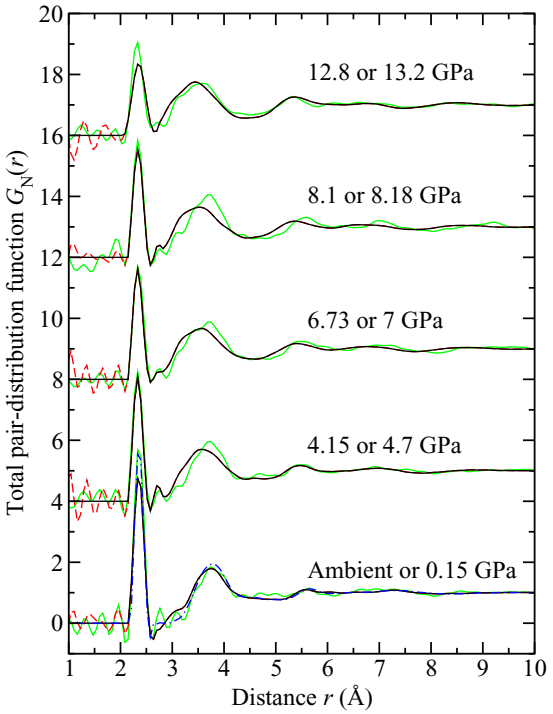

FIG. 7. The pressure dependence of the neutron total pair-distribution function $G_N(r)$ for $GeSe_4$ glass. The solid (black) curves show the Fourier transforms of the spline-fitted measured $S_N(k)$ functions shown in Fig. 6 at ambient pressure, 4.7, 7, 8.1, and 12.8 GPa. The chained (red) curves show the Fourier transform artifacts at r values smaller than the distance of closest approach between two atoms, and oscillate about the calculated $G_N(r) \rightarrow 0 = 0$ limiting values as shown by the solid (black) curves in the small-r region. The chained (blue) curve at ambient pressure shows the Fourier transform of the $S_N(k)$ function given by the chained (blue) curve in Fig. 6. The solid light (green) curves show the Fourier transforms of the FPMD $S_N(k)$ functions (as calculated directly in reciprocal space) at pressures of 0.15, 4.15, 6.73, 8.18, and 13.2 GPa using the same k_{max} values as for the corresponding measured data sets. The high-pressure curves have been offset vertically for clarity of presentation.

homopolar Ge-Ge bonds first contribute to the value of $\bar{n}_{Ge}$ [Fig. 5(c)], manifesting themselves in $g_{GeGe}(r)$ by a small-r feature with peaks at 2.35 and 2.58 Å [Fig. 9(c)]. The majority of Se atoms are involved in Se-Se homopolar bonds across the entire pressure range [Fig. 5(c)].

The second peak at $\simeq$3.75 Å in $G_N(r)$ or $G_X(r)$ at ambient pressure has contributions from all three partial pair-distribution functions but is dominated by $g_{SeSe}(r)$ on account of the large atomic fraction of Se (Sec. II). With increasing pressure, the broadening of the second peak and its shift to small r (Fig. 4) is associated with the appearance and growth of a small-r shoulder at $\simeq$3.25 Å on the second peak in $g_{SeSe}(r)$ [Fig. 9(a)]. At the lowest pressure, there are peaks in $g_{GeGe}(r)$ at 2.97 and 3.68 Å that originate from edge- and corner-sharing Ge-centered tetrahedra, respectively [Fig. 9(c)]. As the pressure increases to 8.18 GPa the first peak shifts to 3.02 Å while the second peak broadens and shifts to 3.44 Å, and at the highest pressure these features merge to give one broad peak at $\sim$3.42 Å. At the lowest pressure, all of the Ge atoms are involved in either corner- or edge-sharing tetrahedra, a participation that reduces to $\simeq$84% at 13.2 GPa [Fig. 5(c)]. Thus $Ge(Se_{1/2})_4$ tetrahedra are preserved as the predominant Ge-centered motifs in $GeSe_4$ glass at pressures ranging from ambient to $\sim$13 GPa.

The pressure-induced evolution of the EDOS is shown in Fig. 10. Our model reproduces the EDOS profile found in previous calculations at ambient pressure [26] and shows a decrease of the band gap energy with increasing pressure [Fig. 11(a)]. This reduction is accompanied by a general broadening of the features in the EDOS, and localized midgap states appear at a pressure of 6.73 GPa. Additional information on the electronic structure is provided by the pressure dependence of the partial pair-distribution function $g_{SeW}(r)$, which describes the correlation between the Se nuclear and WFC positions, where the latter are denoted by W [Fig. 11(b)]. At low pressures, $g_{SeW}(r)$ has a three-peak structure: the first peak at 0.498 Å corresponds to the WFCs for lone-pair valence electrons that do not participate in chemical bonds; the second peak at 1.01 Å corresponds to the WFCs for valence electrons involved in heteropolar Se-Ge chemical bonds; and the third peak at 1.19 Å corresponds to the WFCs for valence

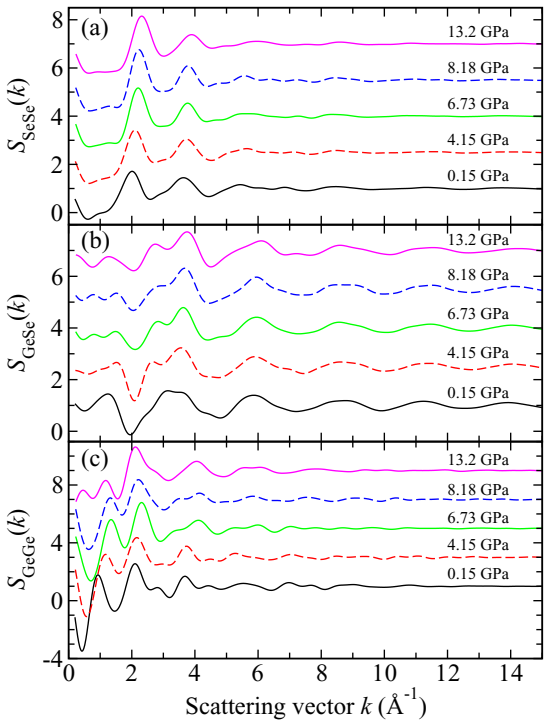

FIG. 8. The pressure dependence of the partial structure factors (a) $S_{\mathrm{SeSe}}(k)$, (b) $S_{\mathrm{GeSe}}(k)$, and (c) $S_{\mathrm{GeGe}}(k)$. The functions were obtained by Fourier-transforming the FPMD $g_{\alpha\beta}(r)$ functions shown in Fig. 9. The high-pressure curves have been offset vertically for clarity of presentation.

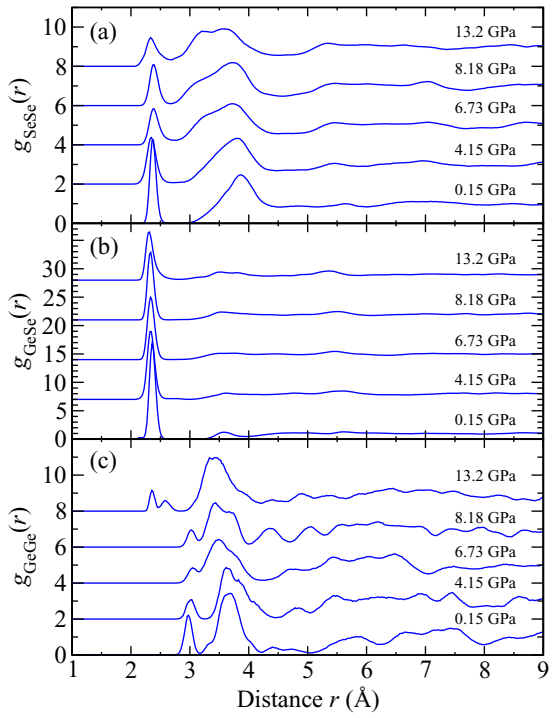

FIG. 9. The pressure dependence of the partial pair-distribution functions (a) $g_{\mathrm{SeSe}}(r)$, (b) $g_{\mathrm{GeSe}}(r)$, and (c) $g_{\mathrm{GeGe}}(r)$ obtained from the FPMD simulations. The high-pressure curves have been offset vertically for clarity of presentation.

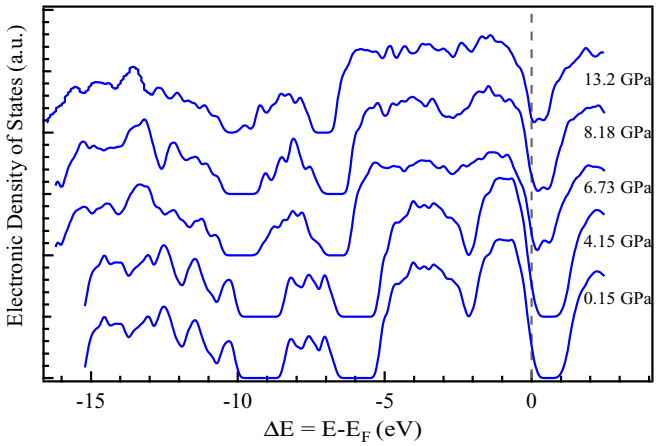

FIG. 10. The pressure dependence of the electronic density of states (EDOS) extracted from the Kohn-Sham eigenvalues. The dashed line corresponds to $\Delta E = E - E_{\mathrm{F}} = 0$ where E_{F} denotes the Fermi energy.

electrons involved in homopolar Se-Se chemical bonds. The position of the second peak shifts towards shorter distances with increasing pressure, corresponding to a larger Ge to WFC separation, which reflects an increase in polar character of the Se-Ge bond. The decrease in intensity of the third peak with increasing pressure is accompanied by a reduction in the fraction of twofold coordinated Se atoms in Se-Se homopolar bonds and by a breakup of the longest Se_n chains (see Sec. VI).

VI. DISCUSSION

Figure 12 shows a representative subset of Ge and Se atoms in an amorphous AB_4 material such as $GeSe_4$. Here, the neighborhood of a *twofold* coordinated B atom consists of either (a) two B neighbors, (b) one A and one B neighbor, or (c) two A neighbors. These configurations are labeled as BB, AB, and AA, respectively. For a chemically ordered network of corner-sharing $A(B_{1/2})_4$ tetrahedra in which every A atom

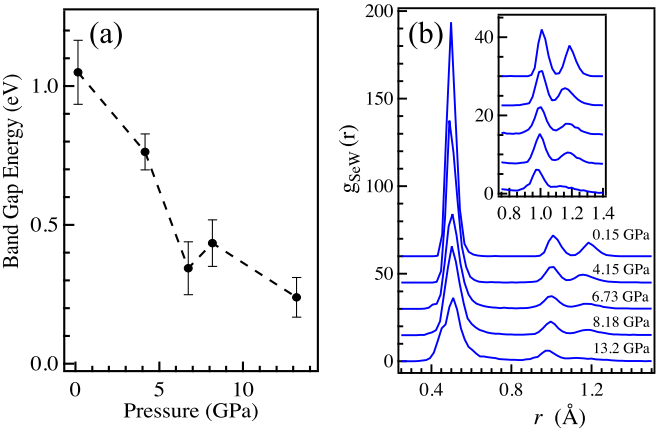

FIG. 11. The pressure dependence of (a) the band gap energy and (b) the partial pair-distribution function $g_{\mathrm{SeW}}(r)$. The error bars in (a) correspond to 95% confidence intervals. The inset in (b) gives a zoom into $g_{\mathrm{SeW}}(r)$ to highlight the peaks that correspond, with increasing r, to the Se-W distances for heteropolar Se-Ge and homopolar Se-Se bonds, respectively.

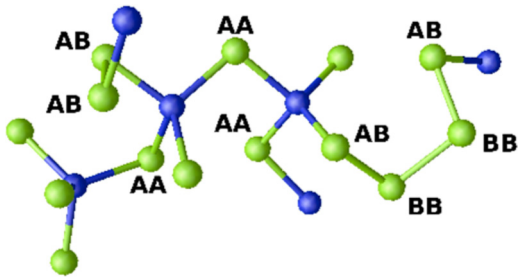

FIG. 12. A representative subset of Ge and Se atoms in amorphous $GeSe_4$ under ambient conditions, where Ge atoms are dark (blue) and Se atoms are light (green). A Se atom in a connection pathway between two Ge atoms is labeled as AA, a Se atom between one Ge atom and one Se atom is labeled as AB, and a Se atom between two Se atoms is labeled as BB.

is connected by B_2 dimers, the fractions of AA, BB, and AB units are 0%, 0%, and 100%, respectively. Departures from this model point to structural variability, which reflects the different conformations that allow for self-organization in the intermediate phase [18,59].

The fractions of ℓ-fold coordinated Ge atoms ($\ell = 3$, 4, or 5) and ℓ-fold coordinated Se atoms ($\ell = 1$, 2, or 3) obtained from the FPMD models for $GeSe_4$ glass are illustrated in Figs. 13(a) and 13(b). The results show that the deviation from a predominantly tetrahedral system at the highest pressure is associated primarily with the formation of 5-fold and 3-fold coordinated Ge and Se atoms, respectively. The fractions of Se atoms at each pressure that are 2-fold coordinated in either an AA, AB, or BB configuration are shown in Fig. 13(c). At the lowest pressure, AB configurations are predominant (∼44%) and the proportions of AA and BB configurations are comparable at ∼27% and ∼28%, respectively. AA connections are found in the four-membered Ge-Se-Ge-Se rings that are formed by edge-sharing $Ge(Se_{1/2})_4$ tetrahedra, and can also link corner-sharing $Ge(Se_{1/2})_4$ tetrahedra. The majority of intertetrahedral connections are, however, formed from Se_n bridges where n is an integer $\geqslant 2$. These findings are consistent with previous FPMD simulations on $GeSe_4$ glass at ambient pressure [59,60] and indicate the absence of a network that is phase separated on the nanoscale into $GeSe_2$ fragments and Se_n chains, a scenario that would be accompanied by a small proportion of AB configurations and by large proportions of both AA and BB configurations [16,21]. The FPMD models find a broad distribution of chain lengths as indicated by Fig. 13(d). The presence of large proportions of AA, BB, *and* AB configurations is confirmed by recent investigations using ^{77}Se nuclear magnetic resonance (NMR) spectroscopy [22,56,61], and the presence of edge-sharing $Ge(Se_{1/2})_4$ tetrahedra with AA configurations is supported by Raman spectroscopy experiments [12,15,21,22].

As the pressure is increased to 8.18 GPa, the proportions of AB, AA, and BB configurations remain comparable at ∼47%, 25%, and 23%, respectively. At the highest pressure of 13.2 GPa there is, however, a drop in the fraction of 2-fold coordinated Se atoms to ∼80% as 3-fold coordinated Se atoms become more prevalent, and the proportions of 2-fold coordinated Se atoms in AB, AA, and BB configurations

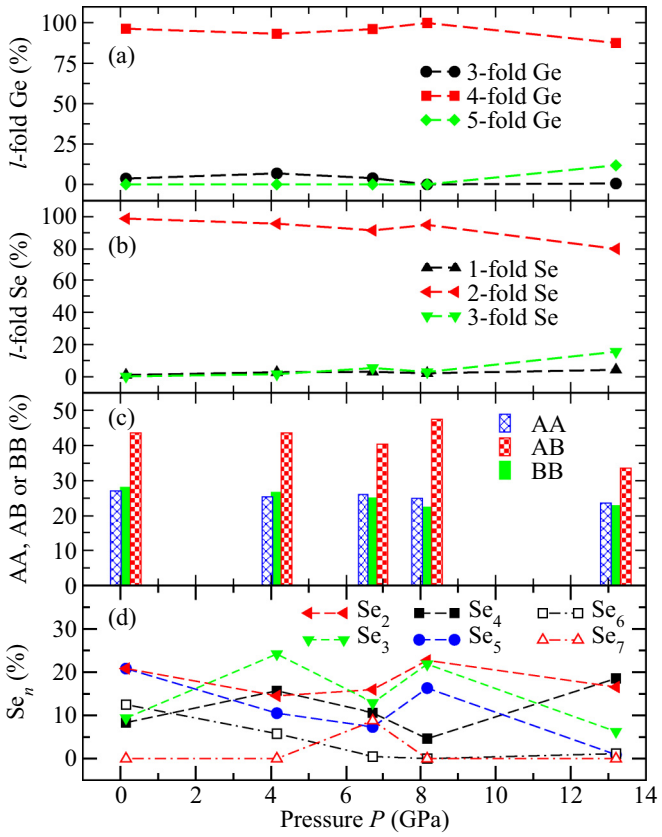

FIG. 13. The pressure-dependent fractions of (a) ℓ-fold coordinated Ge atoms ($\ell = 3$, 4, or 5) and (b) ℓ-fold coordinated Se atoms ($\ell = 1$, 2, or 3) obtained from the FPMD simulations. (c) The pressure-dependent fractions of Se atoms that are 2-fold coordinated in either an AA, AB, or BB configuration. (d) The pressure-dependent fractions of Se atoms that are 2-fold coordinated in Se_n chains where $n = 2$, 3, 4, 5, 6, or 7.

become ∼34%, 24%, and 23%, respectively. Thus, Ge-Se-Se bridges remain the most common intertetrahedral connections but are reduced in number.

Figure 14 shows the pressure dependence of several of the bond angle distributions, where each distribution $B(\theta)$ is normalized by $\sin(\theta)$ to remove the effect of a finite sampling volume [97]. At the lowest pressure, the intratetrahedral Se-Ge-Se bond angle distribution is characterized by a single peak centered at ∼111° (as compared to 109.47° for a regular tetrahedron) that is broadened and shifted to ∼108° at 13.2 GPa, a pressure at which the appearance of 5-fold coordinated Ge atoms [Fig. 13(a)] also leads to a large bond angles of ∼180°. At the lowest pressure, the Ge-Se-Ge bond angle distribution has two peaks located at ∼78.5° and ∼104° that are associated with the Ge atoms belonging to edge- and corner-sharing tetrahedra, respectively. These features merge with increasing pressure to form a broad peak at ∼91° for a pressure of 13.2 GPa. At the lowest pressure, the Ge-Se-Se bond angle distribution has a single peak at ∼98° that broadens and shifts by ∼4° with increasing pressure, accompanying a reduction in the fraction of AB units [Fig. 13(c)]. The Se-Ge-Se and Ge-Se-Se bond angle distributions calculated from the FPMD simulations are in contrast to those obtained

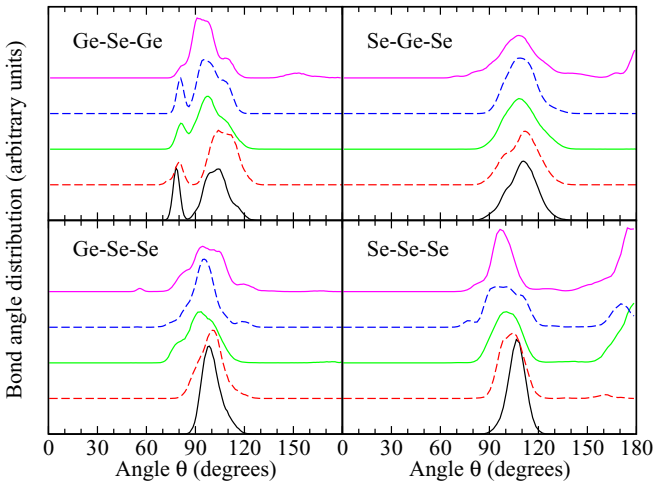

FIG. 14. The pressure dependence of the Ge-Se-Ge, Se-Ge-Se, Ge-Se-Se, and Se-Se-Se bond angle distributions obtained from the FPMD simulations. The curves within a given panel correspond, from bottom to top, to pressures of 0.15, 4.15, 6.73, 8.18, and 13.2 GPa, respectively. The α-β cutoff distances used in these calculations correspond to the first minima in the $g_{\alpha\beta}(r)$ partial pair-distribution functions.

by using the EPSR method [44], where at 1.3 GPa the Se-Ge-Se distribution has two peaks at ∼64° and ∼105° and the Ge-Se-Se distribution has a single peak at ∼58°. Lastly, the Se-Se-Se bond angle distribution in the present work at the lowest pressure has a peak at ∼107° that shifts by 11° to ∼96° as the pressure increases to 13.2 GPa. This change corresponds to a folding of Se_n chains in an attempt to fill the intertetrahedral space, and leads to the appearance of the shoulder at ≃3.25 Å on the low-r side of the second peak in $g_{SeSe}(r)$ [Fig. 9(a)]. The contribution to this distribution at ∼180°, which appears at higher pressures, arises from the bond angles in the polyhedra associated with 3-fold coordinated Se atoms, where the fraction of Se atoms in these polyhedra is ∼15% at 13.2 GPa [Fig. 13(b)].

Figure 15 compares atomistic configurations taken from the FPMD simulations for the lowest and highest pressure points, and helps to summarize the pressure-induced structural changes that occur in $GeSe_4$ glass. The low-pressure structure comprises both corner- and edge-sharing $Ge(Se_{1/2})_4$ tetrahedra

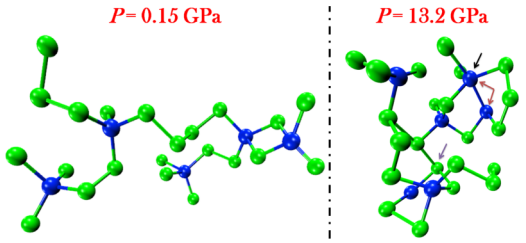

FIG. 15. Atomistic configurations taken from the FPMD simulations of glassy $GeSe_4$ at low and high pressures, where Ge atoms are dark (blue) and Se atoms are light (green). For the high-pressure data set, the arrows point (clockwise from top) to a 5-fold coordinated Ge atom, to the pair of Ge atoms in a homopolar Ge-Ge bond, and to a 3-fold coordinated Se atom.

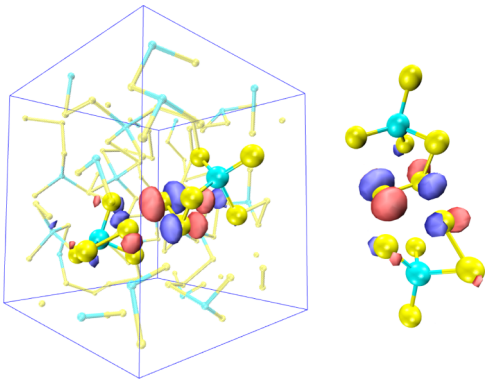

FIG. 16. Snapshots of the most localized Kohn-Sham states close to the band gap (i.e., LUMO) for glassy $GeSe_4$ at 8.18 GPa, where a Se_5 chain is broken into two shorter Se_3 and Se_2 motifs. The LUMO isosurfaces corresponding to values of $+0.04$ Å$^{-3/2}$ and -0.04 Å$^{-3/2}$ are shown in red and blue, respectively. Atoms and bonds are shown by semitransparent spheres and sticks (cyan for Ge, yellow for Se), respectively. The atoms on which the LUMO states are localized, along with several of their nearest neighbors, are highlighted by the larger-sized opaque spheres. The latter are also shown separately to the side of the box, where the Se_3 chain is at the top and the Se_2 dimer is at the bottom.

[Fig. 5(c)], where the corner-sharing configurations dominate. The tetrahedra are linked by AA (Ge-Se-Ge), AB (Ge-Se-Se), and BB (Se-Se-Se) configurations [Fig. 13(c)], where many of the AA conformations correspond to bridges between Ge atoms at the centers of edge-sharing tetrahedra. As the pressure is increased to 8.18 GPa, the network connectivity is largely retained, but there is a broadening of the bond angle distributions (Fig. 14). The shift to smaller angles associated with the Se-Se-Se bond angle distribution manifests itself by the appearance of a low-r shoulder at ≃3.25 Å on the second peak in $g_{SeSe}(r)$ [Fig. 9(a)] that is visible in the total pair-distribution function (Fig. 4). At the highest pressure of 13.2 GPa, 5-fold coordinated Ge atoms and homopolar Ge-Ge bonds begin to appear as 3-fold coordinated Se atoms become more prevalent (Fig. 15). These additional motifs lead to a small increase in $\bar{n}$, giving a value that is in agreement with the measured values from the present neutron diffraction work and from the x-ray diffraction work of Ref. [43] [Fig. 5(b)], but not from the x-ray diffraction work of Ref. [44] where the reported value for $\bar{n}$ is ∼15% larger.

Turning to the electronic structure, the pressure-induced decrease in the band gap energy [Figs. 10 and 11(a)] is in line with experiments that show a semiconductor to metal transition at a pressure in the range of 10–15 GPa [44]. The localized midgap states that appear at pressures at or above 6.73 GPa (Fig. 10) can be characterized in terms of their localization within the glass network, and it is found that the lowest unoccupied molecular orbital (LUMO) is preferentially localized on undercoordinated Se atoms at the termination of Se chains. Figure 16 shows a representative snapshot for the case of glassy $GeSe_4$ at 8.18 GPa, where a Se_5 chain has broken into two shorter Se_3 and Se_2 chains. The fraction of undercoordinated Se atoms is ∼1% at ambient pressure and ∼4.3% at 13.2 GPa.

VII. CONCLUSIONS

The structure of glassy $GeSe_4$ at pressures up to ∼14.4 GPa was investigated in a joint approach that used both neutron diffraction and FPMD. The experimental results are in overall accord with those obtained in the x-ray diffraction work of Skinner *et al.* [43] that show no significant change to the mean coordination number $\bar{n}$ at pressures up to 8.6 GPa. By comparison, in the x-ray diffraction work by Kalkan *et al.* [44], the results were analyzed by using the EPSR method and indicate more substantial structural transformations at pressures below 15 GPa.

The overall results from the present work show that the topological and chemical ordering associated with the ambient pressure network of glassy $GeSe_4$ survives largely intact at pressures up to ∼8 GPa. Although edge-sharing $Ge(Se_{1/2})_4$ tetrahedral motifs in the structure are locally rigid [18,99], the presence of Se_n chains confers the network with a local flexibility that is sufficient to enable significant densification while preserving the basic structural motifs: The increase in density over the ambient to ∼8 GPa pressure range is ∼37% (Fig. 1). The network reorganization maintains a mean coordination number $\bar{n} \simeq 2.4$, the value expected from mean-field constraint-counting theory for a rigid stress-free network. Isostatic networks may therefore remain optimally constrained to avoid stress and retain their favorable glass-forming ability over an extended pressure range. At a pressure around 13 GPa, there is a reduction by ∼15% in the fraction of $Ge(Se_{1/2})_4$ tetrahedra as motifs based on 5-fold coordinated Ge atoms begin to appear, homopolar Ge-Ge bonds form, and there is an increase in the fraction of 3-fold coordinated Se atoms.

Pressure also leads to a decrease in the band gap energy that is accompanied by the appearance of midgap states at a pressure starting from 6.73 GPa. In terms of the chemical bonding, these midgap states originate from undercoordinated Se atoms that terminate Se_n chains, i.e. there is a pressure-induced breakage of Se-Se homopolar bonds in Se_n chains. With increasing pressure, there is also a moderate enhancement in the polar character of the Ge-Se bond.

ACKNOWLEDGMENTS

It is a pleasure to thank Kamil Wezka for help with the experimental work, Ruth Rowlands for measuring the infrared spectra, Alain Bertoni, Jean-Luc Laborier, and Claude Payre for help with the D4c experiment, and Phil Hawkins for help with the PEARL experiment. P.S.S. also thanks Mike Thorpe and Mark Wilson for helpful discussions. Lawrie Skinner and Bora Kalkan are gratefully acknowledged for providing the numerical data sets from Refs. [43] and [44], respectively. The Bath group received support from the EPSRC via Grants No. EP/G008795/1 and No. EP/J009741/1. A.Z. is supported by a Royal Society–EPSRC Dorothy Hodgkin Research Fellowship. The Strasbourg group received support from GENCI for computer facilities (Allocations No. 2015095071 and No. 2015096092), and from the Direction Informatique (Pole HPC) of the University of Strasbourg through a generous allocation of computer time. Part of the HPC resource was funded by the Equipex Equip@Meso project. The lead authors for the theoretical (A.B.) and experimental (K.J.P.) teams contributed equally to this paper.

[1] A. R. Hilton, Appl. Opt. **5**, 1877 (1966).
[2] A. B. Seddon and M. J. Laine, J. Non-Cryst. Solids **213-214**, 168 (1997).
[3] A. Zakery and S. R. Elliott, J. Non-Cryst. Solids **330**, 1 (2003).
[4] D. Lezal, J. Pedlikova, and J. Zavadil, Chalcogenide Lett. **1**, 11 (2004).
[5] J. T. Gopinath, M. Soljačić, E. P. Ippen, V. N. Fuflyigin, W. A. King, and M. Shurgalin, J. Appl. Phys. **96**, 6931 (2004).
[6] A. Zakery and S. R. Elliott, *Optical Nonlinearities in Chalcogenide Glasses and their Applications* (Springer, Berlin, 2007).
[7] T. Kohoutek, T. Wagner, J. Orava, M. Krbal, J. Ilavsky, M. Vlcek, and M. Frumar, J. Non-Cryst. Solids **354**, 529 (2008).
[8] J. Troles, V. Shiryaev, M. Churbanov, P. Houizot, L. Brilland, F. Desevedavy, F. Charpentier, T. Pain, G. Snopatin, and J. L. Adam, Opt. Mater. **32**, 212 (2009).
[9] B. J. Eggleton, B. Luther-Davies, and K. Richardson, Nat. Photonics **5**, 141 (2011).
[10] P. Tronc, N. Bensoussan, A. Brenac, and C. Sebenne, Phys. Rev. B **8**, 5947 (1973).
[11] W. Bresser, P. Boolchand, and P. Suranyi, Phys. Rev. Lett. **56**, 2493 (1986).
[12] S. Sugai, Phys. Rev. B **35**, 1345 (1987).
[13] W. Zhou, M. Paesler, and D. E. Sayers, Phys. Rev. B **43**, 2315 (1991).
[14] X. Feng, W. J. Bresser, and P. Boolchand, Phys. Rev. Lett. **78**, 4422 (1997).
[15] Y. Wang, O. Matsuda, K. Inoue, O. Yamamuro, T. Matsuo, and K. Murase, J. Non-Cryst. Solids **232-234**, 702 (1998).
[16] B. Bureau, J. Troles, M. Le Floch, P. Guénot, F. Smektala, and J. Lucas, J. Non-Cryst. Solids **319**, 145 (2003).
[17] P. S. Salmon, J. Non-Cryst. Solids **353**, 2959 (2007).
[18] A. Sartbaeva, S. A. Wells, A. Huerta, and M. F. Thorpe, Phys. Rev. B **75**, 224204 (2007).
[19] M. T. M. Shatnawi, C. L. Farrow, P. Chen, P. Boolchand, A. Sartbaeva, M. F. Thorpe, and S. J. L. Billinge, Phys. Rev. B **77**, 094134 (2008).
[20] F. Inam, D. N. Tafen, G. Chen, and D. A. Drabold, Phys. Status Solidi B **246**, 1849 (2009).
[21] P. Lucas, E. A. King, O. Gulbiten, J. L. Yarger, E. Soignard, and B. Bureau, Phys. Rev. B **80**, 214114 (2009).
[22] E. L. Gjersing, S. Sen, and B. G. Aitken, J. Phys. Chem. C **114**, 8601 (2010).
[23] E. L. Gjersing, S. Sen, and R. E. Youngman, Phys. Rev. B **82**, 014203 (2010).
[24] S. Hosokawa, I. Oh, M. Sakurai, W.-C. Pilgrim, N. Boudet, J.-F. Bérar, and S. Kohara, Phys. Rev. B **84**, 014201 (2011).
[25] M. Bauchy, M. Micoulaut, M. Celino, S. Le Roux, M. Boero, and C. Massobrio, Phys. Rev. B **84**, 054201 (2011).
[26] M. Micoulaut, A. Kachmar, M. Bauchy, S. Le Roux, C. Massobrio, and M. Boero, Phys. Rev. B **88**, 054203 (2013).
[27] R. Azoulay, H. Thibierge, and A. Brenac, J. Non-Cryst. Solids **18**, 33 (1975).

[28] J. C. Phillips, J. Non-Cryst. Solids **34**, 153 (1979).
[29] M. F. Thorpe, J. Non-Cryst. Solids **57**, 355 (1983).
[30] P. Boolchand, D. G. Georgiev, and B. Goodman, J. Optoelectron. Adv. Mater. **3**, 703 (2001).
[31] P. Boolchand, X. Feng, and W. J. Bresser, J. Non-Cryst. Solids **293-295**, 348 (2001).
[32] S. Bhosle, K. Gunasekera, P. Chen, P. Boolchand, M. Micoulaut, and C. Massobrio, Solid State Commun. **151**, 1851 (2011).
[33] Q. Mei, C. J. Benmore, R. T. Hart, E. Bychkov, P. S. Salmon, C. D. Martin, F. M. Michel, S. M. Antao, P. J. Chupas, P. L. Lee, S. D. Shastri, J. B. Parise, K. Leinenweber, S. Amin, and J. L. Yarger, Phys. Rev. B **74**, 014203 (2006).
[34] K. Wezka, A. Bouzid, K. J. Pizzey, P. S. Salmon, A. Zeidler, S. Klotz, H. E. Fischer, C. L. Bull, M. G. Tucker, M. Boero, S. Le Roux, C. Tugène, and C. Massobrio, Phys. Rev. B **90**, 054206 (2014).
[35] P. S. Salmon and A. Zeidler, J. Phys.: Condens. Matter **27**, 133201 (2015).
[36] L. Properzi, A. Di Cicco, L. Nataf, F. Baudelet, and T. Irifune, Sci. Rep. **5**, 10188 (2015).
[37] F. Wang, S. Mamedov, P. Boolchand, B. Goodman, and M. Chandrasekhar, Phys. Rev. B **71**, 174201 (2005).
[38] P. V. Teredesai, Phys. Chem. Glasses **47**, 240 (2006).
[39] S. M. Antao, C. J. Benmore, B. Li, L. Wang, E. Bychkov, and J. B. Parise, Phys. Rev. Lett. **100**, 115501 (2008).
[40] S. Asokan, M. V. N. Prasad, G. Parthasarathy, and E. S. R. Gopal, Phys. Rev. Lett. **62**, 808 (1989).
[41] M. V. N. Prasad, S. Asokan, G. Parthasarathy, S. S. K. Titus, and E. S. R. Gopal, Phys. Chem. Glasses **34**, 199 (1993).
[42] M. Durandurdu and D. A. Drabold, Phys. Rev. B **65**, 104208 (2002).
[43] L. B. Skinner, C. J. Benmore, S. Antao, E. Soignard, S. A. Amin, E. Bychkov, E. Rissi, J. B. Parise, and J. L. Yarger, J. Phys. Chem. C **116**, 2212 (2012).
[44] B. Kalkan, R. P. Dias, C.-S. Yoo, S. M. Clark, and S. Sen, J. Phys. Chem. C **118**, 5110 (2014).
[45] R. Car and M. Parrinello, Phys. Rev. Lett. **55**, 2471 (1985).
[46] I. Petri, P. S. Salmon, and H. E. Fischer, J. Phys.: Condens. Matter **11**, 7051 (1999).
[47] S. Le Roux, A. Bouzid, M. Boero, and C. Massobrio, J. Chem. Phys. **138**, 174505 (2013).
[48] P. S. Salmon and J. Liu, J. Phys.: Condens. Matter **6**, 1449 (1994).
[49] S. Le Roux, A. Zeidler, P. S. Salmon, M. Boero, M. Micoulaut, and C. Massobrio, Phys. Rev. B **84**, 134203 (2011).
[50] S. Le Roux, A. Bouzid, M. Boero, and C. Massobrio, Phys. Rev. B **86**, 224201 (2012).
[51] I. T. Penfold and P. S. Salmon, Phys. Rev. Lett. **67**, 97 (1991).
[52] I. Petri, P. S. Salmon, and W. S. Howells, J. Phys.: Condens. Matter **11**, 10219 (1999).
[53] I. Petri, P. S. Salmon, and H. E. Fischer, Phys. Rev. Lett. **84**, 2413 (2000).
[54] P. S. Salmon and I. Petri, J. Phys.: Condens. Matter **15**, S1509 (2003).
[55] M. Micoulaut, R. Vuilleumier, and C. Massobrio, Phys. Rev. B **79**, 214205 (2009).
[56] M. Kibalchenko, J. R. Yates, C. Massobrio, and A. Pasquarello, J. Phys. Chem. C **115**, 7755 (2011).
[57] M. Micoulaut, S. Le Roux, and C. Massobrio, J. Chem. Phys. **136**, 224504 (2012).
[58] A. Bouzid and C. Massobrio, J. Chem. Phys. **137**, 046101 (2012).
[59] C. Massobrio, M. Celino, P. S. Salmon, R. A. Martin, M. Micoulaut, and A. Pasquarello, Phys. Rev. B **79**, 174201 (2009).
[60] K. Sykina, E. Furet, B. Bureau, S. Le Roux, and C. Massobrio, Chem. Phys. Lett. **547**, 30 (2012).
[61] K. Sykina, B. Bureau, L. Le Pollès, C. Roiland, M. Deschamps, C. J. Pickard, and E. Furet, Phys. Chem. Chem. Phys. **16**, 17975 (2014).
[62] A. Bouzid, S. Le Roux, G. Ori, M. Boero, and C. Massobrio, J. Chem. Phys. **143**, 034504 (2015).
[63] N. Ramesh Rao, P. S. R. Krishna, S. Basu, B. A. Dasannacharya, K. S. Sangunni, and E. S. R. Gopal, J. Non-Cryst. Solids **240**, 221 (1998).
[64] H. E. Fischer, A. C. Barnes, and P. S. Salmon, Rep. Prog. Phys. **69**, 233 (2006).
[65] T. E. Faber and J. M. Ziman, Philos. Mag. **11**, 153 (1965).
[66] E. Lorch, J. Phys. C **2**, 229 (1969).
[67] P. S. Salmon, J. Phys.: Condens. Matter **18**, 11443 (2006).
[68] A. B. Bhatia and D. E. Thornton, Phys. Rev. B **2**, 3004 (1970).
[69] P. S. Salmon, Proc. R. Soc. London A **437**, 591 (1992).
[70] P. S. Salmon, J. Phys.: Condens. Matter **19**, 455208 (2007).
[71] V. F. Sears, Neutron News **3**, 26 (1992).
[72] J. A. Savage and S. Nielsen, Infrared Phys. **5**, 195 (1965).
[73] S. Klotz, *Techniques in High Pressure Neutron Scattering* (CRC Press, Boca Raton, FL, 2013).
[74] H. E. Fischer, G. J. Cuello, P. Palleau, D. Feltin, A. C. Barnes, Y. S. Badyal, and J. M. Simonson, Appl. Phys. A **74**, S160 (2002).
[75] A. Zeidler, M. Guthrie, and P. S. Salmon, High Press. Res. **35**, 239 (2015).
[76] J. W. E. Drewitt, P. S. Salmon, A. C. Barnes, S. Klotz, H. E. Fischer, and W. A. Crichton, Phys. Rev. B **81**, 014202 (2010).
[77] P. S. Salmon, J. W. E. Drewitt, D. A. J. Whittaker, A. Zeidler, K. Wezka, C. L. Bull, M. G. Tucker, M. C. Wilding, M. Guthrie, and D. Marrocchelli, J. Phys.: Condens. Matter **24**, 415102 (2012).
[78] A. Zeidler, K. Wezka, D. A. J. Whittaker, P. S. Salmon, A. Baroni, S. Klotz, H. E. Fischer, M. C. Wilding, C. L. Bull, M. G. Tucker, M. Salanne, G. Ferlat, and M. Micoulaut, Phys. Rev. B **90**, 024206 (2014).
[79] P. S. Salmon, S. Xin, and H. E. Fischer, Phys. Rev. B **58**, 6115 (1998).
[80] R. J. Angel, in *High-Temperature and High-Pressure Crystal Chemistry* (Reviews in Mineralogy and Geochemistry, Vol. 41, Chap. 2), edited by R. M. Hazen and R. T. Downs (Mineralogical Society of America, Chantilly, VA, 2000), pp. 35–59.
[81] R. Ota, T. Yamate, N. Soga, and M. Kunugi, J. Non-Cryst. Solids **29**, 67 (1978).
[82] J.-P. Guin, T. Rouxel, J.-C. Sangleboeuf, I. Melscoët, and J. Lucas, J. Am. Ceram. Soc. **85**, 1545 (2002).
[83] See http://www.cpmd.org, © 1990–2008 IBM Corp., Armonk, NY, and © 1997–2001 MPI für Festkörperforschung Stuttgart, Stuttgart.
[84] A. D. Becke, Phys. Rev. A **38**, 3098 (1988).
[85] C. Lee, W. Yang, and R. G. Parr, Phys. Rev. B **37**, 785 (1988).
[86] N. Troullier and J. L. Martins, Phys. Rev. B **43**, 1993 (1991).
[87] S. Nosé, Mol. Phys. **52**, 255 (1984).
[88] S. Nosé, J. Chem. Phys. **81**, 511 (1984).
[89] W. G. Hoover, Phys. Rev. A **31**, 1695 (1985).
[90] G. J. Martyna, M. L. Klein, and M. Tuckerman, J. Chem. Phys. **97**, 2635 (1992).

[91] M. Parrinello and A. Rahman, Phys. Rev. Lett. **45**, 1196 (1980).
[92] M. Parrinello and A. Rahman, J. Appl. Phys. **52**, 7182 (1981).
[93] P. Focher, G. L. Chiarotti, M. Bernasconi, E. Tosatti, and M. Parrinello, Europhys. Lett. **26**, 345 (1994).
[94] R. Resta and S. Sorella, Phys. Rev. Lett. **82**, 370 (1999).
[95] N. Marzari and D. Vanderbilt, Phys. Rev. B **56**, 12847 (1997).
[96] M. Celino, S. Le Roux, G. Ori, B. Coasne, A. Bouzid, M. Boero, and C. Massobrio, Phys. Rev. B **88**, 174201 (2013).
[97] A. Zeidler, P. S. Salmon, R. A. Martin, T. Usuki, P. E. Mason, G. J. Cuello, S. Kohara, and H. E. Fischer, Phys. Rev. B **82**, 104208 (2010).
[98] A. K. Soper, Phys. Rev. B **72**, 104204 (2005).
[99] M. Wilson, Phys. Chem. Chem. Phys. **14**, 12701 (2012).